CrossMark

The Detection of Hot Cores and Complex Organic Molecules in the Large Magellanic Cloud

Marta Sewiło[1,13] , Remy Indebetouw[2,3] , Steven B. Charnley[1] , Sarolta Zahorecz[4,5] , Joana M. Oliveira[6] ,
Jacco Th. van Loon[6] , Jacob L. Ward[7], C.-H. Rosie Chen[8] , Jennifer Wiseman[1] , Yasuo Fukui[9], Akiko Kawamura[10] ,
Margaret Meixner[11], Toshikazu Onishi[4] , and Peter Schilke[12]

[1] NASA Goddard Space Flight Center, 8800 Greenbelt Road, Greenbelt, MD 20771, USA; marta.m.sewilo@nasa.gov
[2] Department of Astronomy, University of Virginia, P.O. Box 400325, Charlottesville, VA 22904, USA
[3] National Radio Astronomy Observatory, 520 Edgemont Road, Charlottesville, VA 22903, USA
[4] Department of Physical Science, Graduate School of Science, Osaka Prefecture University, 1-1 Gakuen-cho, Naka-ku, Sakai, Osaka 599-8531, Japan
[5] Chile Observatory, National Astronomical Observatory of Japan, National Institutes of Natural Science, 2-21-1 Osawa, Mitaka, Tokyo 181-8588, Japan
[6] Lennard-Jones Laboratories, Keele University, Staffordshire ST5 5BG, UK
[7] Astronomisches Rechen-Institut, Zentrum für Astronomie der Universität Heidelberg, Mönchhofstr. 12-14, D-69120 Heidelberg Germany
[8] Max-Planck-Institut für Radioastronomie, Auf dem Hügel 69, D-53121 Bonn, Germany
[9] School of Science, Nagoya University, Furo-cho, Chikusa-ku, Nagoya 464-8602, Japan
[10] National Astronomical Observatory of Japan, 2-21-1 Osawa, Mitaka, Tokyo 181-8588, Japan
[11] Space Telescope Science Institute, 3700 San Martin Drive, Baltimore, MD 21218, USA
[12] I. Physikalisches Institut der Universität zu Köln, Zülpicher Str. 77, D-50937 Köln, Germany

Abstract

We report the first extragalactic detection of the complex organic molecules (COMs) dimethyl ether (CH_3OCH_3) and methyl formate (CH_3OCHO) with the Atacama Large Millimeter/submillimeter Array (ALMA). These COMs, together with their parent species methanol (CH_3OH), were detected toward two 1.3 mm continuum sources in the N 113 star-forming region in the low-metallicity Large Magellanic Cloud (LMC). Rotational temperatures ($T_{\rm rot} \sim 130$ K) and total column densities ($N_{\rm rot} \sim 10^{16}$ cm^{-2}) have been calculated for each source based on multiple transitions of CH_3OH. We present the ALMA molecular emission maps for COMs and measured abundances for all detected species. The physical and chemical properties of two sources with COMs detection, and the association with H_2O and OH maser emission, indicate that they are hot cores. The fractional abundances of COMs scaled by a factor of 2.5 to account for the lower metallicity in the LMC are comparable to those found at the lower end of the range in Galactic hot cores. Our results have important implications for studies of organic chemistry at higher redshift.

Key words: astrochemistry – galaxies: star formation – Magellanic Clouds – stars: protostars

1. Introduction

Complex organic molecules (COMs, $\geqslant 6$ atoms including carbon; e.g., CH_3OH, CH_3OCH_3, CH_3OCHO) are widespread in the Milky Way galaxy where they have primarily been found in the environments of young protostars–hot cores and hot corinos (e.g., Herbst & van Dishoeck 2009). Hot cores are compact ($D \lesssim 0.1$ pc), hot ($T_{\rm kin} > 100$ K), dense ($n_{\rm H} > 10^{6-7}$ cm^{-3}) sources (e.g., Kurtz et al. 2000) where ice mantles have recently been removed from dust grains, either by thermal evaporation or sputtering in shock waves. Interstellar COMs may be a chemical link to the prebiotic molecules that were involved in the processes leading to the origin of life (Ehrenfreund & Charnley 2000).

The observed hot core molecules may have their origin in the chemistry of the cold prestellar phase, either through formation in gas-phase reactions followed by freeze-out on the dust, or as products of reactions on the icy mantles of the dust grains (Brown et al. 1988). Grain-surface production could involve atom addition reactions on cold dust (e.g., Charnley & Rodgers 2008) or radical reactions on warm dust during the thermal warm up of the hot core (Garrod & Herbst 2006). Alternatively, COMs and other molecules may be formed in subsequent gas-phase reactions in the hot gas (e.g., Charnley et al. 1992).

In galaxies with subsolar metallicities, questions remain as to the formation efficiency of COMs (e.g., Acharyya & Herbst 2015; Shimonishi et al. 2016a). Apart from the lower elemental abundances of gaseous C, O, and N atoms, low metallicity leads to less shielding, greater penetration of UV photons into dense gas, and consequently warmer dust grains (e.g., van Loon et al. 2010; Oliveira et al. 2011). All of these factors inhibit the formation and survival of COMs.

The Large Magellanic Cloud (LMC) is a nearby dwarf galaxy (50.0 ± 1.1 kpc; Pietrzyński et al. 2013) that presents the opportunity to study COM chemistry in a low-metallicity environment ($Z_{\rm LMC} \sim 0.3$–$0.5\,Z_\odot$; Westerlund 1997) with higher UV fluxes and lower cosmic-ray ionization rates than the Milky Way (e.g., Abdo et al. 2010). Shimonishi et al. (2016b) have claimed a hot core detection toward the LMC young stellar object (YSO) ST11 based on the derived physical conditions and the presence of simple molecules connected to hot gas chemistry (e.g., SO_2 and its isotopologues). Neither methanol or COMs were detected.

Nishimura et al. (2016a) observed seven molecular clouds in the LMC at low spatial resolution (~ 8 pc) and also failed to detect methanol or any COMs. Several transitions of methanol have previously been reported in two star-forming regions in the LMC (N 159W and N 113; Heikkilä et al. 1999; Wang et al. 2009), both included in the Nishimura et al. (2016a) sample, and a few CH_3OH masers are reported in the literature
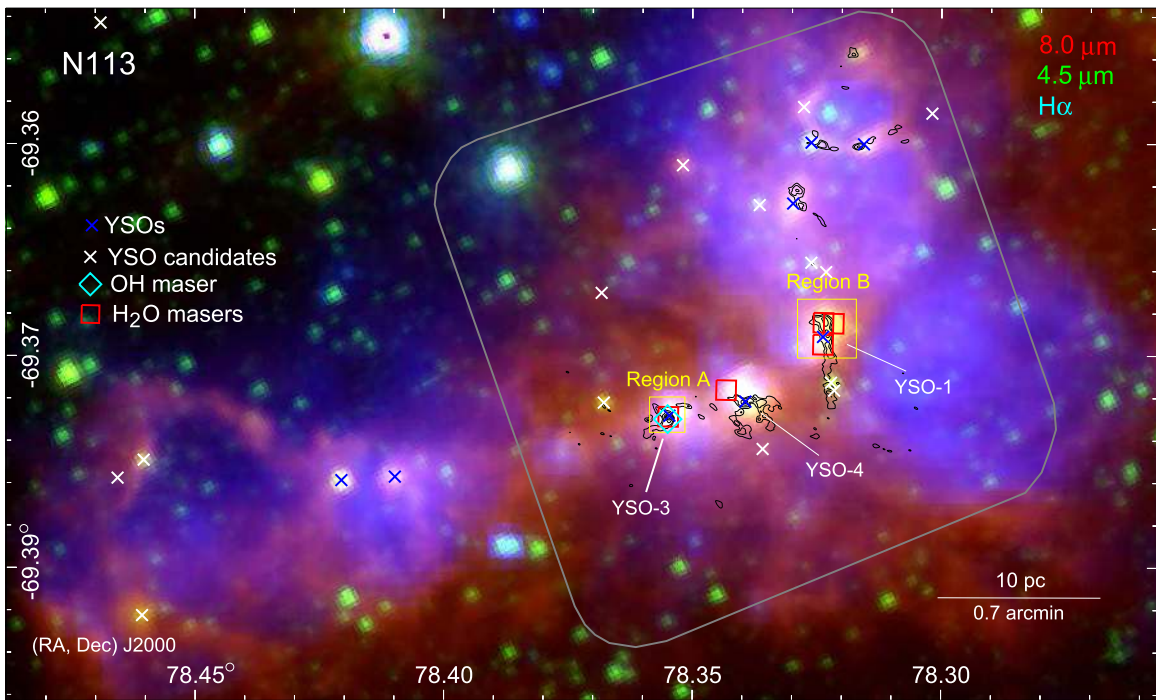

Figure 1. Three-color composite image of N 113 combining the *Spitzer*/SAGE IRAC 8.0 μm (red) and 4.5 μm (green; Meixner et al. 2006), and the MCELS Hα (blue; Smith & MCELS Team 1998) images. The gray rounded rectangle shows an approximate ALMA Band 6 coverage. The positions of the YSOs, YSO candidates, and masers are marked as indicated in the legend. Black contours correspond to the ALMA ^{13}CO (2–1) integrated intensity with contour levels of (10, 20, 40, 60, 80)% of the peak of 3.17 Jy beam^{-1} km s^{-1}. Regions A and B where COMs are detected are indicated with yellow boxes. Source YSO–2 is outside the field of view.

(e.g., Sinclair et al. 1992; Green et al. 2008). The existing studies indicate that the abundance of CH$_3$OH in the LMC is very low, with potentially important general implications for COM formation in low-metallicity galaxies and at high redshift.

The sources observed by Nishimura et al. (2016a) contain large abundances of CCH, a good photodissociation region (PDR) tracer, with the highest CCH column density found in N 113. This suggests that the formation of COMs in the LMC and other low-metallicity galaxies (e.g., IC10; Nishimura et al. 2016b) could be inhibited by the presence of extensive PDRs (Hollenbach & Tielens 1999). Apart from destruction by photolysis, warm dust ($\gtrsim$20 K) leads to inefficient H atom sticking and CO hydrogenation to methanol on grain surfaces (e.g., Watanabe & Kouchi 2008).

In this Letter, we report the first extragalactic detection of the COMs dimethyl ether (CH$_3$OCH$_3$) and methyl formate (CH$_3$OCHO) in the N 113 region of the LMC. We present the Atacama Large Millimeter/submillimeter Array (ALMA) molecular emission maps and measured abundances of the COMs. The relationship to Galactic hot cores and the implications for extragalactic organic chemistry are briefly discussed.

2. The N 113 Star-forming Region

LHA 120–N 113 (N 113; Henize 1956) is one of the most prominent star formation regions in the LMC. It contains one of the most massive ($\sim$10^5 $M_\odot$) and richest giant molecular clouds (GMCs) in the LMC. Its peak CO (1–0) brightness temperature of $\sim$8.1 K is the highest in the MAGMA survey with the Mopra telescope (half-power beam width, HPBW $\sim$ 45$''$; Wong et al. 2011).

The dense molecular gas in the N 113 GMC is clumpy with substructures that are directly revealed by the high volume density tracers HCO$^+$ and HCN (e.g., Seale et al. 2012). N 113 hosts the largest number of H$_2$O and OH masers and the brightest H$_2$O maser in the entire LMC (e.g., Whiteoak & Gardner 1986; Green et al. 2008; Ellingsen et al. 2010), all located within 25$''$ ($\sim$6 pc) from the GMC's CO (1–0) peak.

Current star formation activity in N 113 appears concentrated in the central part of the GMC as indicated by point-like midinfrared emission, maser sources, and compact H II regions, superposed on an extended emission component and aligned in a northwest–southeast direction (see Figure 1). The gas and dust in this central region are compressed by a complex structure of ionized gas bubbles (prominent in the Hα images) created by massive stars in several young clusters (Oliveira et al. 2006). Based on the *Spitzer Space Telescope* and the *Herschel Space Observatory* data, confirmed and candidate Stage 0–II YSOs down to $\sim$3 $M_\odot$ were identified (e.g., Sewiło et al. 2010; Carlson et al. 2012).

At *Spitzer* and *Herschel* wavelengths (3.6–500 μm with 2$''$–38$''$ resolution), N 113 is dominated by emission from three massive (30–40 $M_\odot$; Ward et al. 2016) YSOs associated with high-density molecular clumps, radio continuum emission, and masers: YSO–1 (051317.69–692225.0; Gruendl & Chu 2009), YSO–3 (051325.09–692245.1), and YSO–4 (051321.43–692241.5); see Figure 1. Our *Herschel* spectroscopic data (e.g., [O I], [O III], [C II]) reveal distinct physical conditions around each of these nearby sources (J. M. Oliveira et al., in preparation). *K*-band observations obtained with VLT/SINFONI with 0$''$1 resolution and a field of view of $\sim$3$''$ resolved YSO–3 and YSO–4 into a cluster of multiple components and revealed diverse characteristics of resolved sources (Ward et al. 2016). N 113 is a complex environment where we find clumps ($\sim$1 pc) and cores ($\sim$0.1–0.2 pc) in a range of environments (e.g., strongly influenced by the stellar winds in the west and more quiescent in the east) and at a range of evolutionary stages.

3. ALMA Observations of N 113

N 113 was observed with ALMA in Band 6 as part of project 2015.1.01388.S. The spectral setup observed ^{12}CO (2–1), ^{13}CO (2–1), and C^{18}O (2–1) in narrow windows and additional 2 GHz windows centered on 231.7 and 216.9 GHz.

The data were obtained with the 12 m array on 2016 March 10 and June 16, for a total of 13.1 minutes per mosaic pointing over most of the map, on baselines from 15 to 704 m. It was also observed 19 times with the 7 m Atacama Compact Array (ACA) array between 2015 November 2 and December 17, for a total of 247 minutes per mosaic pointing. The data were calibrated with versions 4.7 through 5.0 of the ALMA pipeline in Common Astronomy Software Applications (CASA; McMullin et al. 2007). Amplitude was calibrated using Uranus, J0538–4405, J0519–4546, and Callisto (different calibrators on different dates). The bandpass was calibrated using J0538–4405, J0522–3627, J0854+2006, J0006–0623, and time-varying gain using J0529–7245 (12 m array) and J0440–6952 (7 m array).

Sensitivity of 0.1 mJy per $0\rlap.{''}87 \times 0\rlap.{''}54$ ($\sim$0.21 $\times$ 0.13 pc) beam was achieved in the continuum. Continuum was subtracted in the *uv* domain from each line spectral window, and the 7 m and 12 m data were simultaneously imaged and deconvolved interactively. Sensitivity of 3.8 mJy per $0\rlap.{''}98 \times 0\rlap.{''}62$ ($\sim$0.24 $\times$ 0.15 pc) beam was achieved in the 216.9 GHz cube with 1.09 MHz (1.5 km s^{-1}) channels, and 2.9 mJy per $0\rlap.{''}88 \times 0\rlap.{''}58$ ($\sim$0.21 $\times$ 0.14 pc) beam in 2.0 MHz (2.6 km s^{-1}) channels at 231.7 GHz.

The distribution of our project's main targeted bright lines over the entire N 113 region will be discussed in a future publication, as the scope of this Letter is the complex organic molecules located in two small regions in the center of N 113 (Regions A and B in Figure 1).

4. Results

4.1. 1.3 mm Continuum Emission

We have identified multiple 1.3 mm continuum sources in both Regions A and B (see Figure 2). We have assigned identification numbers to all of the continuum peaks that are associated with the molecular or H30α line emission in the order from the brightest to faintest. There is a number of the continuum peaks that are less significant and/or not associated with the molecular or H30α line emission that will be discussed in a follow-up paper. COMs have been detected toward sources A1 and B3. Both sources are associated with H$_2$O masers and A1 also with an OH maser (within the positional uncertainties). Only one SINFONI K-band source (N113–YSO01) has been detected at 1.3 mm (B2).

There is some evidence for a small difference in the evolutionary stage between A1 and B3. B3 is brighter than A1 in DCN, which indicates that it is younger. The DCN/HCN ratio will drop rapidly with time in hot gas, irrespective of the origin of DCN in the gas phase or on ice. The abundance of all deuterated species decreases with time (Fontani et al. 2011); in hot cores, they are fossils of the earlier, colder evolutionary phases. The more mature nature of A1 is supported by an association with the OH maser.

We measured the continuum surface brightness for A1 and B3 in the continuum image centered at 224.6 GHz by fitting the sources with Gaussians, as well as measuring the value of the brightest pixel. The weighted average of the fitted and manually measured peaks (0.58 ± 0.09 K and 0.29 ± 0.02 K

for A1 and B3, respectively) was used to calculate the dust column density. The dust optical depth was calculated by assuming that the dust temperature equals the fitted CH$_3$OH kinetic temperature (see Section 4.2). The largest source of uncertainty is the choice of dust emissivity used to calculate column density from optical depth. We use values calculated specifically for the LMC by Galliano et al. (2011), albeit on somewhat larger scales ($\geqslant$10 pc): $N(\mathrm{H_2})/\tau_{\mathrm{dust}} = 1.8 \times 10^{26}$ cm^{-2}. If dust has coagulated on the small scales probed by ALMA, the dust emissivity could be higher, hydrogen column densities lower, and organic molecule abundances higher than we quote here. We determined $N(\mathrm{H_2})$ of $(8.0 \pm 1.2) \times 10^{23}$ cm^{-2} and $(7.0 \pm 0.9) \times 10^{23}$ cm^{-2} for A1 and B3, respectively. The source diameters are about the beam size; thus, under the assumption of spherical symmetry, these column densities correspond to the number densities of $\sim$1.6 $\times$ 10^6 cm^{-3} and $\sim$1.4 $\times$ 10^6 cm^{-3}, respectively.

4.2. Spectral Line Analysis

The spectra for A1 and B3 are shown in Figure 3. We detected COMs (CH$_3$OH, CH$_3$OCHO, and CH$_3$OCH$_3$), sulfur-bearing molecules (SO$_2$, H$_2$S, SiO, OCS, ^{13}CS, and ^{33}SO), *c*-C$_3$H$_2$, and DCN (see Table 1). We have carried out the line identification with the MADCUBAIJ software (Martín et al. 2011; Rivilla et al. 2016), which uses the JPL[14] and CDMS[15] molecular line databases. This software provides theoretical synthetic spectra of the different molecules under local thermodynamic equilibrium (LTE) conditions, taking into account the individual opacity of each line. To identify a molecule, the detectable lines in the observed spectra predicted by the LTE analysis must be present, with the relative intensities of the different transitions consistent with the LTE analysis.

We used the results of the rotational diagram analysis (e.g., Goldsmith & Langer 1999) of CH$_3$OH as the initial parameters for the spectral line modeling using MADCUBAIJ. We utilized six CH$_3$OH transitions with a range of upper energy levels ($E_{\mathrm{u}} \sim$ 56–508 K; see Figure 4). This analysis assumes the gas is in LTE and the lines are optically thin. We obtained the rotational temperatures and total column densities (T_{rot}, N_{rot}) of (134 ± 6 K, $1.6 \pm 0.1 \times 10^{16}$ cm^{-2}) and (131 ± 15 K, $6.4 \pm 0.8 \times 10^{15}$ cm^{-2}) for A1 and B3, respectively. The synthetic spectra corresponding to these parameters are shown in Figure 3. The uncertainties for the calculated temperature and column density values are the formal fit uncertainties from the least squares fits performed by MADCUBAIJ.

Assuming that all molecular species observed toward A1/B3 are located in the same region as methanol, we estimate their column densities using the same T_{rot} as for methanol (see Table 1). To investigate how the results would change if we assumed a different value of T_{rot}, we calculated column densities for T_{rot} of 100, 150, 200, and 250 K. In general, column densities increase gradually with increasing T_{rot}, and they are not larger than a factor of $\sim$2 than those listed in Table 1 for any molecule at $T_{\mathrm{rot}} = 250$ K. At 100 K, column densities are in general up to $\sim$20% lower.

A non-detection of CH$_3$OH in N 113 by Nishimura et al.'s (2016a) single-dish observations can be explained by the fact that they covered Region B only. Region B harbors the fainter
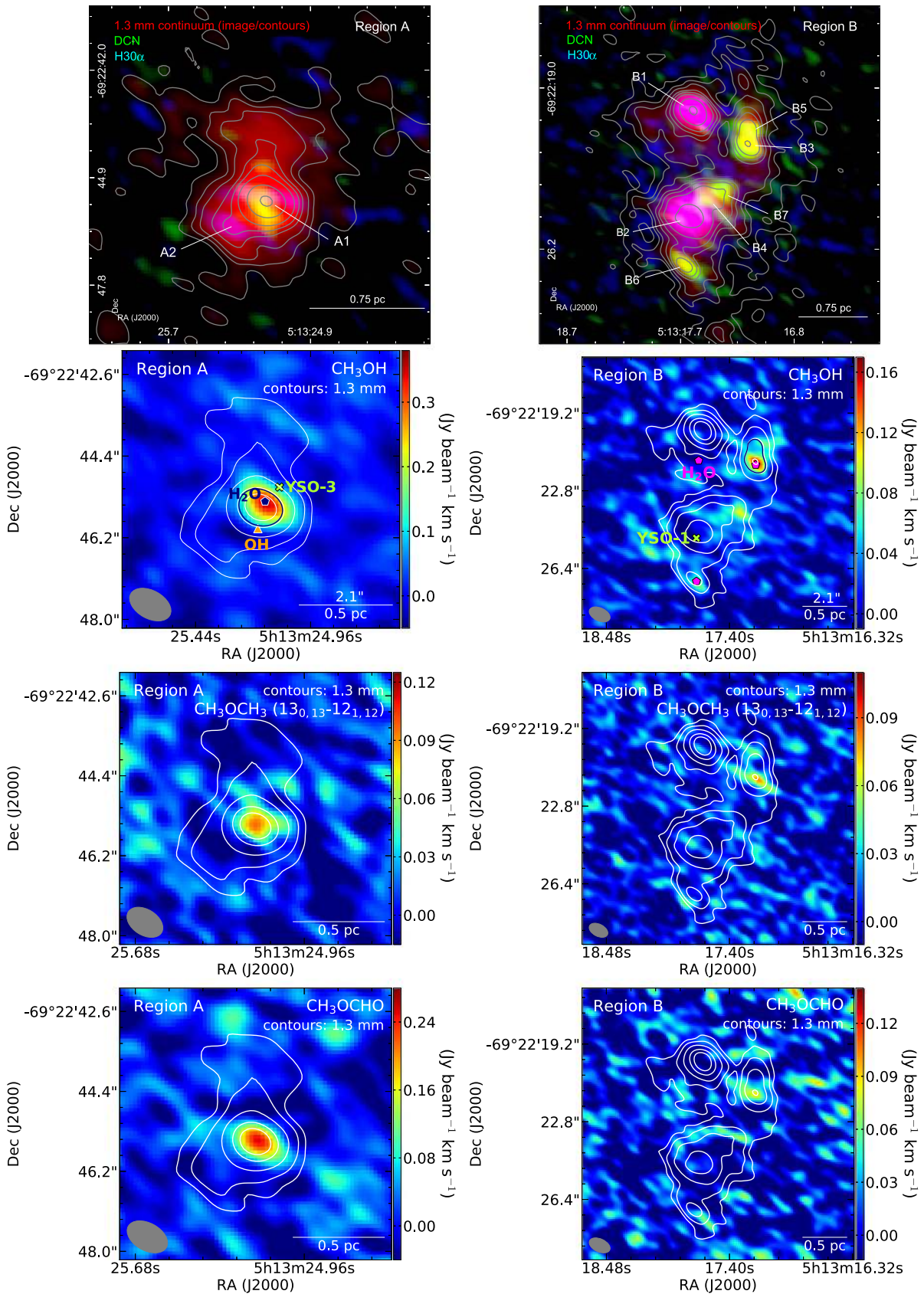
---

[14] http://spec.jpl.nasa.gov/
[15] http://www.astro.uni-koeln.de/cdms

Figure 2. Top panels: the three-color mosaics combining the 1.3 mm continuum (red), DCN (green), and H30α (blue) images for Regions A (left) and B (right). The 1.3 mm continuum contour levels are (3, 6, 9, 15, 20, 30, 60, 120) × 0.1 mJy beam^{-1} (1σ). Second row: the CH$_3$OH integrated intensity image for Regions A and B with selected 1.3 mm continuum contours overlaid for reference. The CH$_3$OH images were made using the channels corresponding to all CH$_3$OH transitions in the 216.9 GHz spectral window. The positions of the H$_2$O (pentagons) and OH (triangle) masers and *Spitzer* YSOs ("×") are indicated. The areas enclosed by navy contours were used to extract the spectra shown in Figure 3. The CH$_3$OCH$_3$ (13$_{0,13}$–12$_{1,12}$) and CH$_3$OCHO (integrated over all transitions) images for Regions A and B are shown in the third and fourth rows.
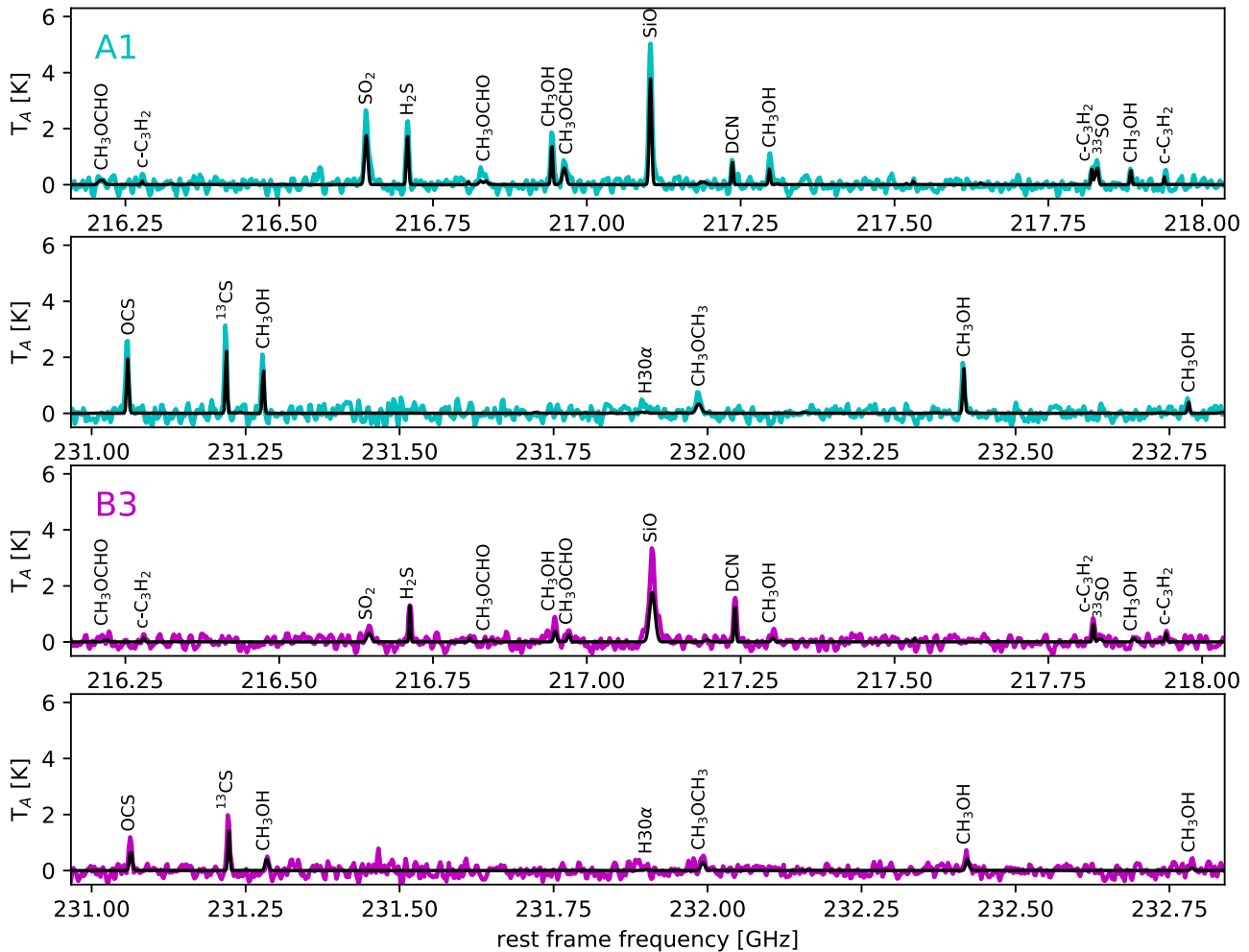
Figure 3. Spectra for A1 (top two panels, cyan) and B3 (bottom panels, purple) for two Band 6 spectral windows. The spectra were integrated over the area enclosed by the 1.3 mm continuum emission contour at the level of 50% of the peak for the corresponding source (see Figure 2). The synthetic spectra are shown in black. The molecular transitions listed in Table 1 are indicated.

and smaller of the two sources with CH_3OH detection, suffering larger effects from beam dilution. The single-dish observations of Wang et al. (2009) that detected methanol in N 113 had a similar sensitivity; however, they covered both Regions A and B. The CH_3OH column density estimated by Wang et al. (2009; $\sim 10^{13}$ cm^{-2}) is lower than that based on the ALMA data, likely the effect of the beam dilution. Only with ALMA can the clumpy structure of methanol be revealed.

5. Discussion

Both A1 and B3 resemble classic hot cores–dense condensations of molecular gas surrounding the massive star formation sites. They are compact ($D \sim 0.17$ pc) and hot ($T_{rot} \sim 130$ K), as evidenced by the high excitation lines of methanol with rotation temperatures similar to Galactic hot cores at the lower end of the T_{rot} range (e.g., Kurtz et al. 2000). A1 and B3 are slightly larger than "typical" Galactic hot cores, but their number densities and column densities are consistent with those of known hot cores, they are hot enough to release ice mantles, they show emission from COMs, and they are associated with masers; all of these properties support the classification of A1 and B3 as hot cores.

Some fainter methanol emission is detected in other locations in Region B (see Figure 2); however, it is unclear

whether that traces physically distinct sources or shocked lobes of the outflows.

The detection of SiO demonstrates that shock sputtering of dust and ice may be as important as thermal evaporation for initiating the chemical evolution in these hot cores (e.g., Charnley & Kaufman 2000; Viti et al. 2001). A SiH_4 (i.e., non-shock) origin for SiO is possible (Mackay 1996), but it requires that hot cores contain abundances of O_2 that are significantly above the observed upper limits obtained with *Herschel* (e.g., Liseau et al. 2012; Yıldız et al. 2013).

The detection of CH_3OH indicates that the dust was once cold enough for CO hydrogenation to proceed and the observed DCN is probably a frozen gas-phase remnant of this cold cloud chemistry (Brown & Millar 1989).

Using the CH_3OH and H_2 column densities derived above, we calculate the fractional abundance of CH_3OH of $(2.0 \pm 0.3) \times 10^{-8}$ and $(9.1 \pm 1.7) \times 10^{-9}$ for A1 and B3, respectively. These CH_3OH fractional abundances are over an order of magnitude larger than an upper limit estimated for the candidate hot core ST11 by Shimonishi et al. (2016b). The (CH_3OCH_3, CH_3OCHO) fractional abundances are $(2.2 \pm 0.7, 1.4 \pm 0.4) \times 10^{-9}$ for A1 and $(1.7 \pm 0.7, <0.5) \times 10^{-9}$ for B3. The (CH_3OCH_3, CH_3OCHO) abundances with respect to CH_3OH are $(0.11 \pm 0.03, 0.07 \pm 0.01)$ and $(0.19 \pm 0.07, <0.05)$ for A1 and B3, respectively.

Table 1
Molecular Line Transitions Detected toward A1 and B3

Species	Transition	Frequency (GHz)	E_u[a] (K)	Detection[b] A1	Detection[b] B3	I_{int} (K km s^{-1})[c] A1	I_{int} (K km s^{-1})[c] B3	Column Density[d,e] (cm^{-2}) A1	Column Density[d,e] (cm^{-2}) B3
CH$_3$OH v$_t$ = 0[f]	$5_{1,4}$–$4_{2,2}$	216.94560	55.87102	+	+	13.8(0.5)	3.4(0.5)		
CH$_3$OH v$_t$ = 1	$6_{1,5}$–$7_{2,6}$	217.299205	373.92517	+	+	8.2(0.2)	2.2(0.2)		
CH$_3$OH v$_t$ = 0	$20_{1,19}$–$20_{0,20}$	217.88639	508.37582	+	–	4.5(0.3)	⋯	1.6(0.1) × 10^{16}	6.4(0.8) × 10^{15}
CH$_3$OH v$_t$ = 0	$10_{2,9}$–$9_{3,6}$	231.28110	165.34719	+	+	7.3(0.4)	1.8(0.4)		
CH$_3$OH v$_t$ = 0	$10_{2,8}$–$9_{3,7}$	232.41859	165.40178	+	+	8.1(0.4)	3.7(0.4)		
CH$_3$OH v$_t$ = 0	$18_{3,16}$–$17_{4,13}$	232.78350	446.53167	+	+	2.5(0.2)	2.7(0.2)		
CH$_3$OCHO v = 0	$18_{2,16}$–$17_{2,15}$ E	216.83020	105.67781	+?	–	1.5(0.2)	⋯		
CH$_3$OCHO v = 0	$18_{2,16}$–$17_{2,15}$ A	216.83889	105.66730	+?	–	2.2(0.2)	⋯		
CH$_3$OCHO v = 0	$20_{1,20}$–$19_{1,19}$ E	216.96476	111.49762	+	+?			1.1(0.2) × 10^{15}	<3.4 × 10^{14}
CH$_3$OCHO v = 0	$20_{1,20}$–$19_{1,19}$ A	216.96590	111.48055	+	+?	6.2(0.3)	2.4(0.1)		
CH$_3$OCHO v = 0	$20_{0,20}$–$19_{0,19}$ E	216.96625	111.49826	+	+?				
CH$_3$OCHO v = 0	$20_{0,20}$–$19_{0,19}$ A	216.96742	111.48048	+	+?				
CH$_3$OCH$_3$	$13_{0,13}$–$12_{1,12}$ EE	231.98782	80.92308	+	+	6.0(0.6)	3.9(1.0)	1.8(0.5) × 10^{15}	1.2(0.4) × 10^{15}
c-C$_3$H$_2$ v = 0	$3_{3,0}$–$2_{2,1}$	216.27876	19.47	+	+	0.5(0.1)	0.9(0.1)		
c-C$_3$H$_2$ v = 0	$6_{0,6}$–$5_{1,5}$	217.82215	38.61	+	+				
c-C$_3$H$_2$ v = 0	$6_{1,6}$–$5_{0,5}$	217.82215	38.61	+	+	2.0(0.3)	4.8(0.4)	3.7(0.7) × 10^{13}	5.6(1.0) × 10^{13}
c-C$_3$H$_2$ v = 0	$5_{1,4}$–$4_{2,3}$	217.94005	35.42	+?	+	1.3(0.2)	2.9(0.3)		
^{33}SO	6_5–5_4, F = 9/2–7/2	217.82718	34.67135	+	+?				
^{33}SO	6_5–5_4, F = 11/2–9/2	217.82983	34.67292	+	+?				
^{33}SO	6_5–5_4, F = 13/2–11/2	217.83177	34.67502	+	+?	9.2(0.2)	2.9(0.3)	1.4(0.2) × 10^{14}	⋯[g]
^{33}SO	6_5–5_4, F = 15/2–13/2	217.83264	34.67766	+	+?				
SO$_2$ v = 0	$22_{2,20}$–$22_{1,21}$	216.64330	248.44117	+	+	18.7(1.4)	3.6(0.6)	3.9(0.4) × 10^{15}	9.4(1.7) × 10^{14}
H$_2$S	$2_{2,0}$–$2_{1,1}$	216.71044	83.98035	+	+	11.9(0.8)	7.5(0.3)	1.2(0.1) × 10^{15}	5.6(0.4) × 10^{14}
SiO	5–4	217.10498	31.25889	+	+	29.7(1.1)	30.8(1.7)	6.9(0.3) × 10^{13}	7.0(0.5) × 10^{13}
DCN v = 0	3–2	217.238	20.85164	+	+	3.4(0.2)	7.6(0.2)	1.0(0.1) × 10^{13}	1.8(0.1) × 10^{13}
OCS v = 0	19–18	231.06098	110.89923	+	+	12.4(1.0)	4.5(0.3)	8.4(0.9) × 10^{14}	4.1(0.3) × 10^{14}
^{13}CS	5–4	231.2210	33.29138	+	+	12.8(0.5)	7.9(0.6)	6.4(0.3) × 10^{13}	4.1(0.4) × 10^{13}

Notes.

[a] E_u is the upper level energy of the transition.

[b] The symbols in these columns indicate a detection ("+"), a tentative detection ("+?"), or a non-detection ("−") of a given molecular line transition.

[c] I_{int} is the integrated line intensity.

[d] The CH$_3$OH column densities and temperatures were derived based on modeling of multiple CH$_3$OH transitions (see the text). Column densities of other molecules were estimated assuming the same temperature as for methanol.

[e] For molecules with multiple transitions, all the transitions were used to estimate a total column density.

[f] A typical line width for the strongest methanol line is ∼5 km s^{-1} for A1 and ∼8 km s^{-1} for B3.

[g] ^{33}SO lines for B3 are too faint to get a good fit.

The abundances of COMs detected in N 113 are comparable to those found at the lower end of the range in Galactic hot cores (e.g., Herbst & van Dishoeck 2009; Taquet et al. 2016), when scaled by a factor of 2.5 to account for the lower metallicity in the LMC (assuming $Z_{LMC} = 0.4\,Z_\odot$). Thus, the chemistry of COMs detected in N 113 is similar to that of the Galaxy, indicating that regions where they exist are likely shielded from UV radiation (see Cuadrado et al. 2017). Both grain reactions on warm dust and post-desorption ion–molecule chemistry could form CH$_3$OCH$_3$ and CH$_3$OCHO (Garrod & Herbst 2006; Taquet et al. 2016).

We have also detected several S-bearing molecules in both cores. In A1 and B3, the H$_2$S/CH$_3$OH ratios are respectively 0.075 ± 0.008 and 0.088 ± 0.013, whereas the OCS/CH$_3$OH ratios are 0.053 ± 0.007 and 0.064 ± 0.009. These ratios are almost indistinguishable between A1 and B3, supporting the idea that these molecules were formed in ices during the N113 prestellar phase. OCS is known to be present in interstellar ices (Boogert et al. 2015) and, although H$_2$S has not yet been
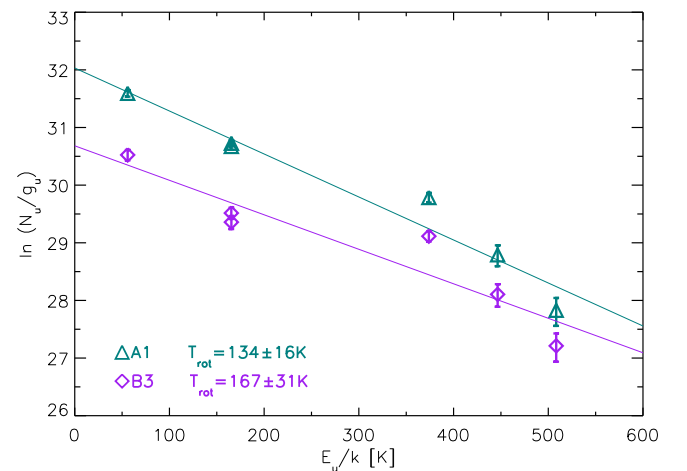

Figure 4. Rotational diagram of CH$_3$OH detected toward A1 and B3. The results of the rotational diagram analysis were used as the initial parameters for the MADCUBAIJ modeling.

confirmed, cold grain-surface chemistry, involving reactions of S atoms with atomic hydrogen and CO (or oxidation of CS), is likely to be the origin of these molecules in the N 113 cores.

SO and SO_2 could also originate from ice chemistry (they are detected in cometary ices; Calmonte et al. 2016), but they may also form in post-shock gas that is enriched in OH through neutral–neutral reactions (Hartquist et al. 1980). Alternatively, chemical models show that all the S-bearing molecules, including SO and SO_2, could be formed in post-evaporation gas-phase reactions starting from evaporated ices containing H_2S (Charnley 1997). In this case, comparison of calculated and observed SO/SO_2, H_2S/SO_2, and H_2S/SO ratios could be used as a chemical clock for the age of the core. We will explore this issue in a future publication.

Finally, c-C_3H_2 could either be formed by ion–molecule chemistry in the cool ambient medium or, like CCH, be in a PDR region, where it may be produced in the photodestruction of larger refractory organic (PAH) molecules (Guzmán et al. 2014).

6. Conclusions

We see the effective formation of COMs under subsolar metallicity conditions in two hot cores discovered in the LMC. The COMs observed in the N 113 hot cores could either originate from grain-surface chemistry or in post-desorption gas chemistry. Of the S-bearing molecules detected, it is likely that H_2S and OCS formed on grains; SO and SO_2 also could have originated from ice chemistry or formed in gaseous neutral reactions. The presence of SiO indicates that shock chemistry may also be playing a role. Future observations of LMC cores and detailed chemical modeling will be necessary to determine the relative contribution from each process. Studying the chemistry of the interstellar medium as a function of metallicity is important to understand the chemical evolution of the universe.

ORCID iDs

Marta Sewiło https://orcid.org/0000-0003-2248-6032
Remy Indebetouw https://orcid.org/0000-0002-4663-6827
Steven B. Charnley https://orcid.org/0000-0001-6752-5109
Sarolta Zahorecz https://orcid.org/0000-0001-6149-1278
Joana M. Oliveira https://orcid.org/0000-0002-0861-7094
Jacco Th. van Loon https://orcid.org/0000-0002-1272-3017
C.-H. Rosie Chen https://orcid.org/0000-0002-3925-9365
Jennifer Wiseman https://orcid.org/0000-0002-1143-6710
Akiko Kawamura https://orcid.org/0000-0001-7813-0380
Toshikazu Onishi https://orcid.org/0000-0001-7826-3837
Peter Schilke https://orcid.org/0000-0003-2141-5689

References

Abdo, A. A., Ackermann, M., Ajello, M., et al. 2010, A&A, 512, A7
Acharyya, K., & Herbst, E. 2015, ApJ, 812, 142
Boogert, A. C. A., Gerakines, P. A., & Whittet, D. C. B. 2015, ARA&A, 53, 541
Brown, P. D., Charnley, S. B., & Millar, T. J. 1988, MNRAS, 231, 409
Brown, P. D., & Millar, T. J. 1989, MNRAS, 237, 661
Calmonte, U., Altwegg, K., Balsiger, H., et al. 2016, MNRAS, 462, 253
Carlson, L. R., Sewiło, M., Meixner, M., Romita, K. A., & Lawton, B. 2012, A&A, 542, A66
Charnley, S. B. 1997, ApJ, 481, 396
Charnley, S. B., & Kaufman, M. J. 2000, ApJ, 529, 111
Charnley, S. B., & Rodgers, S. D. 2008, SSRv, 138, 59
Charnley, S. B., Tielens, A. G. G. M., & Millar, T. J. 1992, ApJ, 399, 71
Cuadrado, S., Goicoechea, J. R., Cernicharo, J., et al. 2017, A&A, 603, A124
Ehrenfreund, P., & Charnley, S. B. 2000, ARA&A, 38, 427
Ellingsen, S. P., Breen, S. L., Caswell, J. L., Quinn, L. J., & Fuller, G. A. 2010, MNRAS, 404, 779
Fontani, F., Palau, A., Caselli, P., et al. 2011, A&A, 529, 7
Galliano, F., Hony, S., Bernard, J.-P., et al. 2011, A&A, 536, A88
Garrod, R. T., & Herbst, E. 2006, A&A, 457, 927
Goldsmith, P. F., & Langer, W. D. 1999, ApJ, 517, 209
Green, J. A., Caswell, J. L., Fuller, G. A., et al. 2008, MNRAS, 385, 948
Gruendl, R. A., & Chu, Y. 2009, ApJS, 184, 172
Guzmán, V. V., Pety, J., Gratier, P., et al. 2014, FaDi, 168, 103
Hartquist, T. W., Dalgarno, A., & Oppenheimer, M. 1980, ApJ, 236, 182
Heikkilä, A., Johansson, L. E. B., & Olofsson, H. 1999, A&A, 344, 817
Henize, K. G. 1956, ApJS, 2, 315
Herbst, E., & van Dishoeck, E. F. 2009, ARA&A, 47, 427
Hollenbach, D. J., & Tielens, A. G. G. M. 1999, RvMP, 71, 173
Kurtz, S., Cesaroni, R., Churchwell, E., Hofner, P., & Walmsley, C. M. 2000, in Protostars and Planets IV, ed. V. Mannings, A. P Boss, & S. S. Russell (Tucson, AZ: Univ. Arizona Press), 299
Liseau, R., Goldsmith, P. F., Larsson, B., et al. 2012, A&A, 541, 73
Mackay, D. D. S. 1996, MNRAS, 278, 62
Martín, S., Krips, M., Martín-Pintado, J., et al. 2011, A&A, 527, A36
McMullin, J. P., Waters, B., Schiebel, D., Young, W., & Golap, K. 2007, in ASP Conf. Ser. 376, Astronomical Data Analysis Software and Systems XVI, ed. R. A. Shaw, F. Hill, & D. J. Bell (San Francisco, CA: ASP), 127
Meixner, M., Gordon, K. D., Indebetouw, R., et al. 2006, AJ, 132, 2268
Nishimura, Y., Shimonishi, T., Watanabe, Y., et al. 2016a, ApJ, 818, 161
Nishimura, Y., Shimonishi, T., Watanabe, Y., et al. 2016b, ApJ, 829, 94
Oliveira, J. M., van Loon, J. T., Stanimirovíc, S., & Zijlstra, A. A. 2006, MNRAS, 372, 1509
Oliveira, J. M., van Loon, J. Th., Sloan, G. C., et al. 2011, MNRAS, 411, 36
Pietrzyński, G., Graczyk, D., Gieren, W., et al. 2013, Natur, 495, 76
Rivilla, V. M., Fontani, F., Beltrán, M. T., et al. 2016, ApJ, 826, 161
Seale, J. P., Looney, L. W., Wong, T., et al. 2012, ApJ, 751, 42
Sewiło, M., Indebetouw, R., Carlson, L. R., et al. 2010, A&A, 518, L73
Shimonishi, T., Dartois, E., Onaka, T., & Boulanger, F. 2016a, A&A, 585, A107
Shimonishi, T., Onaka, T., Kawamura, A., & Aikawa, Y. 2016b, ApJ, 827, 72
Sinclair, M. W., Carrad, G. J., Caswell, J. L., Norris, R. P., & Whiteoak, J. B. 1992, MNRAS, 256, 33

Smith, R. C. & MCELS Team 1998, PASA, 15, 163

Taquet, V., Wirström, E. S., & Charnley, S. B. 2016, ApJ, 821, 46

van Loon, J. Th., Oliveira, J. M., Gordon, K. D., Sloan, G. C., & Engelbracht, C. W. 2010, AJ, 139, 1553

Viti, S., Caselli, P., Hartquist, T. W., & Williams, D. A. 2001, A&A, 370, 1017

Wang, M., Chin, Y.-N., Henkel, C., Whiteoak, J. B., & Cunningham, M. 2009, ApJ, 690, 580

Ward, J. L., Oliveira, J. M., van Loon, J. T., & Sewiło, M. 2016, MNRAS, 455, 2345

Watanabe, N., & Kouchi, A. 2008, PrSS, 83, 439

Westerlund, B. E. 1997, The Magellanic Clouds (New York: Cambridge Univ. Press)

Whiteoak, J. B., & Gardner, F. F. 1986, MNRAS, 222, 513

Wong, T., Hughes, A., Ott, J., et al. 2011, ApJS, 197, 16

Yıldız, U. A., Acharyya, K., Goldsmith, P. F., et al. 2013, A&A, 558, 58